J. Fluid Mech. (2010), *vol.* 643, *pp.* 137–162.
doi:10.1017/S0022112009992072

Numerical and experimental studies of the rolling sphere wake

B. E. STEWART[1,2]†, M. C. THOMPSON[1], T. LEWEKE[2] AND K. HOURIGAN[1,3]

[1]Fluids Laboratory for Aeronautical and Industrial Research (FLAIR), Department of Mechanical and Aerospace Engineering, Monash University, Melbourne, Victoria 3800, Australia

[2]Institut de Recherche sur les Phénomènes Hors Equilibre, CNRS/Universités Aix-Marseille, 49 rue Frédéric Joliot-Curie, BP 146, F-13384 Marseille cedex 13, France

[3]Division of Biological Engineering, Monash University, Melbourne, Victoria 3800, Australia

(Received 1 March 2009; revised 5 September 2009; accepted 7 September 2009)

A numerical and experimental investigation is reported for the flow around a rolling sphere when moving adjacent to a plane wall. The dimensionless rotation rate of the sphere is varied from forward to reversed rolling and the resulting wake modes are found to be strongly dependent on the value of this parameter. Results are reported for the Reynolds number range $100 < Re < 350$, which has been shown to capture the unsteady transitions in the wake. Over this range of Reynolds number, both steady and unsteady wake modes are observed. As the sphere undergoes forward rolling, the wake displays similarities to the flow behind an isolated sphere in a free stream. As the Reynolds number of the flow increases, hairpin vortices form and are shed over the surface of the sphere. However, for cases with reversed rotation, the wake takes the form of two distinct streamwise vortices that form around the sides of the body. These streamwise structures in the wake undergo a transition to a new unsteady mode as the Reynolds number increases. During the evolution of this unsteady mode, the streamwise vortices form an out-of-phase spiral pair. Four primary wake modes are identified and a very good qualitative agreement is observed between the numerical and experimental results. The numerical simulations also reveal the existence of an additional unsteady mode that is found to be unstable to small perturbations in the flow.

1. Introduction

This study reports the flows resulting from the combined effects of body rotation and the presence of a nearby wall. It is relevant to the situation for which frictional or lubrication effects cause spherical particles to roll or slide along a bounding surface. Previously, only a limited number of studies have considered these combined effects on the flow dynamics. In this study, particular attention is given to the effect of body rotation and wall effects on the observed flow transitions and wake structures. There are various motivations for this work. One is to try to better understand and model particle–wall interactions for particle-laden flows, where there is some evidence that spherical particles can roll forward or backwards near a wall depending on the fluid rheology (see references below), and the forces on particles are an important

† Email address for correspondence: stewart.bronwyn01@gmail.com

component of bulk multiphase models. Another is from biological fluid dynamics, in which rolling/tumbling mobile cells such as platelets and white blood cells interact with surface endothelial cells to initiate a clotting or immune response (e.g. Woollard *et al.* 2008; Jackson 2007).

When a rotational motion is imposed on the sphere, the non-dimensional rotation rate may be defined as

$$\alpha = \frac{D\omega}{2U}, \tag{1.1}$$

where ω is the angular velocity of the sphere and D is the sphere diameter. In the frame of reference attached to the sphere centre, U is the velocity of the free-stream fluid.

Previous studies have shown that at Reynolds number, $Re = UD/\nu = 210$, where ν is the kinematic viscosity, the axisymmetric wake behind the fixed sphere in an unbounded flow undergoes a regular (steady–steady) transition to an asymmetric flow via a supercritical transition (Ghidersa & Dušek 2000). The regular transition leads to the development of a two-tailed wake and studies by Johnson & Patel (1999), Ghidersa & Dušek (2000) and Thompson, Leweke & Provansal (2001) describe the double tail as being composed of a counter-rotating vortex pair. These two vortices impose an induced velocity on each other, which causes them to be convected away from the streamwise centreline of the sphere. Johnson & Patel (1999) speculate that the transition to a non-axisymmetric flow is due to the low pressure core of the axisymmetric toroidal vortex becoming unstable, resulting in an azimuthal pressure gradient that opens up the separation region behind the sphere and allows the flow of fluid to pass through.

Experiments have observed a periodic undulation in the asymmetric wake just prior to the onset of vortex shedding at $270 < Re < 280$ (Taneda 1956; Magarvey & Bishop 1961; Sakamoto & Haniu 1995; Ormières & Provansal 1999). The stability analyses also indicate that the unsteady flow emerges via a supercritical Hopf bifurcation in this range of Reynolds number (Ghidersa & Dušek 2000; Thompson *et al.* 2001; Schouveiler & Provansal 2002). For $Re > 280$, fully formed vortex shedding takes place via the formation of hairpin vortices over one side of the fixed sphere and this flow retains a planar symmetry until $Re > 350$ (Mittal 1999). Throughout this study, the Reynolds number is restricted to the range over which the above transitions occur. However, the nature of the transitions is in some instances significantly altered by the introduction of rotation and a nearby wall.

In general, for an unconstrained sphere moving adjacent to a plane wall in a Newtonian fluid, any observed rotation has been in the positive (normal) direction and of a relatively low magnitude (Cherukat & McLaughlin 1990; Zeng, Balachandar & Fischer 2005). However, in fluids with non-Newtonian properties and for spheres in a strong shear flow or between nearby walls, the accelerating fluid away from the wall can bring about a reversed rotation of the sphere. This type of rotation results in the sphere translating down the wall but rotating as if rolling upwards (Humphrey & Murata 1992; Liu *et al.* 1993).

One of the investigations to examine the free rotation of a near-wall sphere at higher Re was that by Zeng *et al.* (2005). They carried out simulations for the flow around a translating and rotating sphere for $Re \leqslant 300$. The sphere was positioned at different distances to the wall. The smallest of these distances was equal to a gap of 0.25 diameters. At moderate Re they observed small rates of positive rotation, which aided the flow through the gap region. The small effect of rotation on the

drag was consistent with the low Re findings of Cox & Hsu (1977) and Cherukat & McLaughlin (1994). Furthermore, the lift coefficients up to $Re = 100$ agree well with those of Takemura & Magnaudet (2003).

Overall, Zeng *et al.* (2005) found the effect of free rotation on the lift and drag forces of the sphere to be small. However, near the wall, the drag coefficient is increased above that occurring for an unbounded uniform flow. A limited number of flow structures are also described, and the formation of a double-threaded wake is reported. Prior to the formation of this double thread, the flow has an imposed asymmetry due to the presence of the nearby wall. Furthermore, the transition to the double-threaded mode occurs at Re lower than that for the regular bifurcation behind an isolated sphere, and the Re of transition is found to depend on the wall distance. Following this change in the wake structure, a dramatic increase in the overall coefficient of the lift is observed, which is dominated by the pressure rather than the viscous component.

Zeng *et al.* (2009) extended this research to examine gap ratios down to 0.005 sphere diameters, which is equal to the gap studied in this paper. Their main focus was on the forces on a sphere in a shear flow in the steady regime, but they did examine the forces on a particle moving at a uniform velocity near a wall, which is one of the cases examined here. Indeed, this provides a useful validation case for the current study.

When unsteady flow commences, the shedding takes the form of hairpin vortices and loops, as for the single-sided shedding observed behind an isolated sphere. The asymmetry of the geometry fixes the plane of symmetry normal to the wall and the force resulting from the shedding is also in the wall-normal direction.

Zeng *et al.* (2005) found that the proximity of the wall has two competing effects on the flow. The viscous effects act to delay the onset of unsteady flow, while the asymmetry produced in the wake can enhance it. This is reflected in the critical Re of transition. As the sphere is located increasingly closer to the wall, the Re of transition to unsteady flow decreases to values below that observed for the isolated sphere but always remains above 250. However, as the sphere moves from a gap ratio of 0.5 to 0.25, the critical Re rapidly increases to above 300.

An additional effect of the near-wall flow is the possibility for a thin lubrication layer to appear in the fluid near the contact region. Furthermore, the low pressure that forms in this contact region can drop below the vapour pressure of the fluid, leading to the development of cavitation bubbles in the flow. The presence of these bubbles can affect the relative motion of the body and cause a slipping action that prevents normal rolling (Prokunin 2007).

Having observed cavitation experimentally between the sphere and the wall, Prokunin (2004, 2007) developed a theoretical model to describe the motions of a sphere with cavitation. It is found that when the cavitation force pushing the sphere away from the wall is greater than the wall-normal particle weight, a contactless steady sphere motion may be observed. A rotation rate of $\alpha = 0.2$ is predicted for a wide range of wall inclinations. This was less than 30 % of the value of α predicted when cavitation was not taken into account. Ashmore, del Pino & Mullin (2005) observed a similar trend in α when lubrication effects were present for a sphere moving along a wall at low Re. Although α does reach a value of unity (indicating normal rolling), the majority of results appear to asymptote to $\alpha \approx 0.2$ for increasing wall angles. Furthermore, results by Seddon & Mullin (2008) with a sphere placed inside a rotating drum also found α values to lie between 0.2 and 0.25 when cavitation was present.

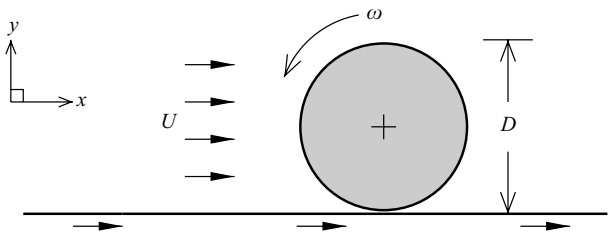

FIGURE 1. Schematic of the problem under consideration.

This study aims to extend the knowledge on the flow structures that result when a rotating sphere is adjacent to a wall. The rotation rates chosen vary from the normal 'no-slip' motion to sliding and a combination of the two. Reversed rotation rates have been considered not only because they are of fundamental interest but also following reports that this type of motion is observed in shear flows and non-Newtonian fluids. Furthermore, useful information may be gained on the effect of such reversed rotation on the drag force and the stability of the wake.

2. Problem definition and methodology

A schematic of the problem under consideration is shown in figure 1. The frame of reference is attached to the centre of the sphere and the inlet flow and lower boundary are moving from left to right at constant velocity, U. The x-axis is aligned to the streamwise direction and the flow is defined in terms of the Reynolds number

$$Re = \frac{UD}{\nu}, \tag{2.1}$$

where ν is the kinematic viscosity of the fluid. The second key parameter used throughout this study is the rotation rate, as defined in (1.1). Positive α is in the direction shown in figure 1, and the selected values of rotation rate range from no-slip rolling in the intuitive sense ($\alpha = 1$) to reversed rolling ($\alpha = -1$). The investigation focuses on five discrete values of the rotation rate, being $\alpha = 1$, 0.5, 0, -0.5 and -1, although some smaller intermediate values are also reported.

Values of the coefficient of drag, C_D, and the Strouhal number, St, have also been reported throughout this study. These have been defined according to

$$C_D = \frac{8F_D}{\rho U^2 \pi D^2}, \tag{2.2}$$

where F_D is the drag force resulting from the pressure and viscous forces acting on the sphere surface, and $St = fD/U$, where f is the wake frequency.

2.1. *Numerical method and validation*

This numerical scheme solves the viscous, incompressible Navier–Stokes equations. These comprise the equations governing momentum transfer:

$$\frac{\partial \boldsymbol{u}}{\partial t} = -(\boldsymbol{u}\cdot\nabla)\boldsymbol{u} - \frac{1}{\rho}\nabla P + \frac{1}{\rho}\nabla\cdot\mu\nabla\boldsymbol{u} \tag{2.3}$$

and continuity,

$$\nabla\cdot\boldsymbol{u} = 0, \tag{2.4}$$

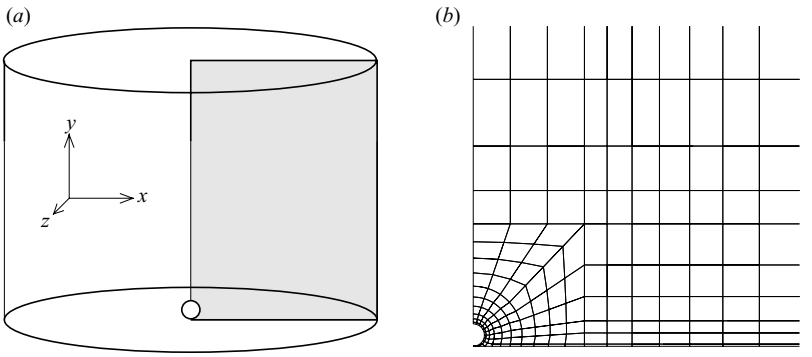

FIGURE 2. Orientation of the axisymmetric geometry with the mesh plane shown in grey (*a*) and a sample of the macro-element mesh in the region near the sphere (*b*).

in the fluid flow. Equations (2.3) and (2.4) are given in vector form, where $\boldsymbol{u}(x, y, z, t) = (u, v, w)$ is the velocity vector, ρ is the fluid density, $\boldsymbol{P}$ is the scalar pressure field and μ is the dynamic viscosity.

The numerical scheme uses a spectral-element method with iterative time-splitting, and the scheme has previously been validated with flows around a variety of geometries including cylinders and spheres (Sheard, Thompson & Hourigan 2004; Ryan, Thompson & Hourigan 2005, 2007; Thompson *et al.* 2006; Leontini, Thompson & Hourigan 2007). The iterative time-stepping allows a relaxation of the time-step constraints that are associated with the present geometry (specifically the small elements in the near-contact region between the sphere and the wall) and enhances the stability of the scheme. Results of the simulations are presented in the non-dimensional form with the relevant variables normalized by the body diameter and the free-stream velocity. Likewise, the time is non-dimensionalized according to $\tau = tU/D$.

A fractional-step method, first developed by Chorin (1968), is used for the temporal discretization. The approach adopted here follows closely that given by Karniadakis, Israeli & Orszag (1991). The method consists of separating the Navier–Stokes equations into convection, pressure and diffusion terms, and integrating these terms in separate sub-steps. Using this method, the errors typically associated with time-splitting techniques have been reduced and the method provides second-order time accuracy for the velocity field. The fractional-step method forms the inner loop of the iterative temporal integration scheme described in Thompson *et al.* (2006).

To construct the three-dimensional space, the two-dimensional mesh is expanded into 128 Fourier planes around the symmetry axis located perpendicular to the wall, as indicated in figure 2, where the grey region indicates a sample plane corresponding to the two-dimensional mesh. A section of the mesh showing the increased resolution of the macro-elements near the sphere surface is also shown in figure 2 and this resolution was maintained for a distance of $30D$ downstream.

For the spatial discretization, Lagrange polynomials of order $N - 1$ are used to represent the solution variables within each macro-element of the mesh, leading to a set of $N \times N$ internal node points. Dirichlet boundary conditions are used to specify the velocity at all external boundaries and on the sphere surface. For $\alpha = 0$, when the sphere has no rotation, a no-slip condition is defined, in which all velocity components reduce to zero at the body surface. Due to numerical constraints, i.e. the potential collapse of the macro-element immediately adjacent to the axis beneath the sphere,

	$Re = 50$, $\alpha = 1$		$Re = 50$, $\alpha = -1$		$Re = 200$, $\alpha = 1$		$Re = 300$, $\alpha = -1$	
N	C_D	St	C_D	St	$\bar{C}_D$	St	$\bar{C}_D$	St
4	1.818	–	2.132	–	0.9168	0.1131	0.8806	0.1630
5	1.820	–	2.135	–	0.9232	0.1133	0.8847	0.1643
6	1.824	–	2.138	–	0.9267	0.1133	0.8845	0.1646

TABLE 1. Spatial resolution for the flow around the sphere with $\alpha = \pm 1$.

it is necessary to impose a small displacement ($< 1\,\%$ of the diameter) between the sphere boundary and the wall. The width of this gap is fixed at $0.005D$ and the effect of variations in this small distance is discussed later.

The convergence of the drag coefficient and the Strouhal number was tested and results are reported for the upper and lower limits of Reynolds numbers at the two extremes of the rotation rate. These limits are $Re = 50$ and 200 for $\alpha = 1$ and $Re = 50$ and 300 for $\alpha = -1$. The high Re flow results in two different unsteady wake modes, while at the lower Re limit the flow remains steady.

The mesh used throughout this study consists of 320 macro-elements with dimensions of $x = 100D$ from the sphere centre to the inlet/outlet boundary and $y = 150D$ to the transverse boundary. Increasing these dimensions by a further $50D$ in each direction was found to result in a variation in C_D of less than 1 % for $Re = 50$. Likewise, for the higher Reynolds number limits, the Strouhal number and the mean drag coefficient, $\bar{C}_D$, of the unsteady flow vary by less than 1 % in each case. The flow is therefore considered to be insensitive to the boundary placement in this case.

To check for the convergence of the simulations with respect to the spatial resolution, the order of the interpolating polynomials is varied from third to fifth order. Values of the resulting drag and the Strouhal number are shown in table 1. Increasing the polynomial order from $N = 4$ shows a small monotonic increase in St. However, for all values of N tested, the Strouhal number was within 1 % and the spatial resolution was found to be sufficient. All future simulations are therefore run with $N \geqslant 4$. Since $N = 6$ provides the highest resolution but does not lead to prohibitive run times, it is therefore used for the remainder of the simulations. The difference in St values for $\alpha = 1$ and -1 in table 1 reflects the fact that two different wake modes occur. The form of these modes are discussed in more detail in § 3.3.

As mentioned above, the gap distance between the sphere and the plane wall was fixed at $0.005D$. This was near the lower limit of what was required for successful computations. A series of sensitivity studies for different values of α were carried out with a gap ratio of $0.004D$ for the unsteady flow regimes at the upper Re limits. In those cases, the 20 % reduction in gap ratio resulted in a less than 0.2 % change in St. In addition, lubrication theory predicts that there is a weak logarithmic dependence of the drag coefficient on gap ratio, even at finite Reynolds number. This was checked at $Re = 50$ for gap ratios of 0.004, 0.005 and 0.010 for the non-rotating sphere case. The logarithmic dependence was indeed observed, and all the drag values were within 3 % of the approximate fit supplied by Zeng *et al.* (2009). Note that while there may be a weak drag singularity as the gap ratio approaches zero, both numerical and experimental observations suggest that the wake structure is not sensitive to gap ratio. Hence, it is assumed that a gap ratio of $G/D = 0.005$ gives an adequate approximation for the flow around the sphere in contact with the wall.

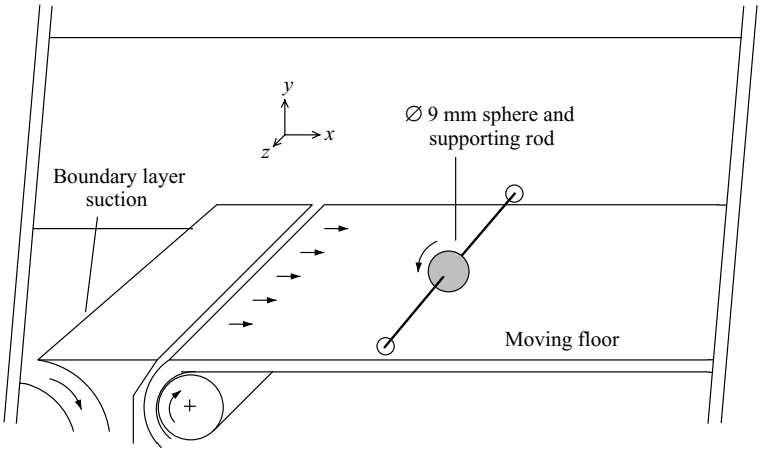

FIGURE 3. Test section of the water tunnel showing the sphere mount location adjacent to the moving floor and upstream boundary-layer suction.

2.2. *Experimental method*

In conjunction with the numerical simulations, an experimental study was also undertaken. The experiments were carried out in a water tunnel equipped with a moving floor and boundary-layer suction. A schematic of the experimental set-up is shown in figure 3. A sphere of diameter 9 mm was supported mid-stream by a supporting rod of diameter 1.5 mm and the rotation of the sphere was driven from one side using a stepper motor. The choice of the rod thickness was a compromise between structural stability and minimizing the effect on the sphere wake. Since shedding begins at a Reynolds number of 47, this means that shedding from the cylindrical rods should not be expected except for $Re \gtrsim 280$. This is towards the upper limit of Reynolds numbers studied experimentally. The moving floor was independently controlled by a separate stepper motor and two continuous flow pumps were used for the boundary-layer suction and free-stream flow. The speed of the moving floor and the boundary-layer suction were both carefully calibrated to match the free-stream velocity.

At the upstream end of the moving floor, a small velocity deficit is present that has developed following the boundary-layer suction. However, the combined effects of the moving floor and the free-stream velocity rapidly act to eliminate this deficit prior to the flow reaching the sphere. More details of velocity profiles throughout the test section may be found in Stewart (2008).

A fluoresceine dye was injected into the flow upstream of the sphere, either on the moving floor or through a narrow tube positioned in the free stream far from the sphere. The dye was then illuminated with the light from an argon laser, allowing visualization of the wake either as a volume or in a plane. Videos of the unsteady flows were also obtained, allowing the Strouhal number to be calculated. For the set of experiments, the Reynolds number was varied between approximately 80 and 350. For the rolling case, the sphere was actually in contact with the surface, while for the other cases, it was positioned as close as possible to the surface without touching. This was done by adjusting the vertical position until the sphere just touched the surface and then backing off the adjustment mechanism slightly until it was no longer touching. It was difficult to determine the exact gap but a reasonable estimate is that

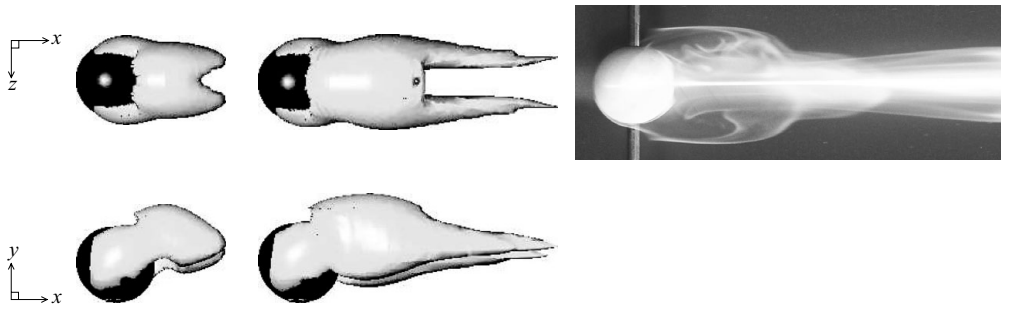

(*a*) $Re = 50$. (*b*) $Re = 100$. (*c*) Experimental results at $Re = 100$.

FIGURE 4. Structures in the wake of the forward-rolling sphere as determined by simulations (*a*) and experiments (*b*). Surface contours in (*a*) and (*b*) show the zero contour of λ_2 (Jeong & Hussain 1995) and are shown from above (top) and from the side (bottom). (*c*) shows an experimental volume dye visualization of the wake.

it was within 2 % of the diameter. More details of the experimental method can be found in Stewart *et al.* (2008).

3. Results and discussion

3.1. *Steady flow*

For all rotation rates studied, the wake remains steady at the lower Reynolds number limit and the structure varies continuously with α. The wake of the forward-rolling sphere ($\alpha > 0$) is characterized by a compact recirculation zone immediately behind the body, and the resulting wake structures for $\alpha = 1$ are shown in figure 4. The vortical structures in the numerical simulations have been visualized by plotting the zero-value isosurface of the λ_2 field defined in Jeong & Hussain (1995). The structure of the wake is in good agreement with what is observed in experiments (figure 4*c*); however, the simulations reveal additional detail that is not apparent in the experimental visualization. Figure 4(*a*) and (*b*) shows that the recirculation zone behind the sphere forms into two streamwise vortices at a short distance downstream. These structures are quite weak at $Re = 50$ but increase in strength with increasing Re. When viewed from the side, the numerical results also show that the wake is displaced away from the wall and towards the top of the sphere. The twin-tailed structure in the wake of figure 4(*b*) is similar to the asymmetric wake observed behind a sphere in an unbounded flow for $210 < Re < 270$ (Johnson & Patel 1999; Ghidersa & Dušek 2000; Thompson *et al.* 2001). In this instance, the nearby wall acts to break the symmetry of the flow and fix the orientation of the wake.

The wake of the sphere undergoing reversed rolling ($\alpha = -1$) has a different structure to that described above, although it may be the result of a continuous, rather than discontinuous, change in wake structure as the rotation rate is varied. When $\alpha < 0$, the motion of the sphere assists the flow passing over the top of the body and two regions of swirling flow are created at either side of the sphere. This forms a counter-rotating streamwise vortex pair that remains stable as it travels downstream. This structure is observed in both numerical simulations and experiments and differs significantly from the wake reported above for $\alpha > 0$. Examples of the numerical and experimental results are shown in figure 5. It can be seen that the compact recirculation zone immediately behind the sphere is absent and the streamwise centreline of the wake

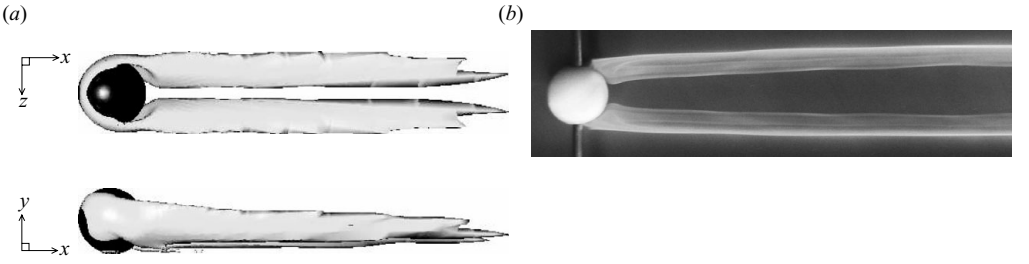

FIGURE 5. Results for the steady sphere wake at $Re = 100$ and $\alpha = -1$, showing the presence of two streamwise vortices that form around the sides of the sphere. The isosurfaces are the same as defined for figure 4. Comparisons from the numerical simulations (*a*) with the experimental flow visualization (*b*). The counter-rotating trailing pair is such that the self-advection is towards the wall.

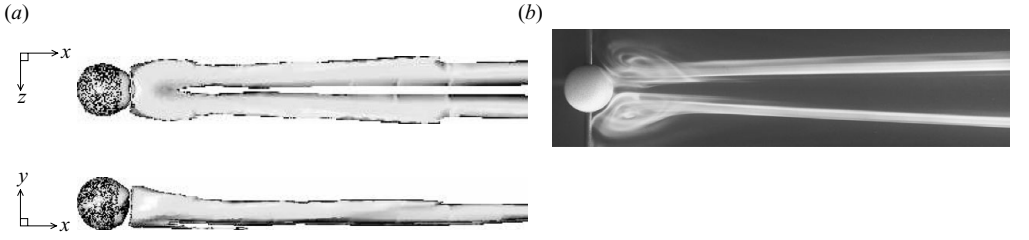

FIGURE 6. Numerical (*a*) and experimental (*b*) results for the steady wake behind the non-rotating sphere at $Re = 200$. This wake has similarities to those occurring behind the sphere during both forward and reverse rolling. The counter-rotating trailing pair is such that the self-advection is towards the wall.

is characterized by a region of relatively undisturbed flow. Unlike for the forward-rolling sphere, the streamwise vortices in this instance remain adjacent to the wall and separate slightly as they move downstream. This is primarily due to a reversal in the direction of rotation of the streamwise vortices that shall be discussed in more detail later.

The wake of the non-rotating sphere is a combination of the two modes described above and is shown in figure 6 at $Re = 200$. When $\alpha = 0$, the vorticity is generated over the entire sphere surface, rather than being concentrated at the sides of the sphere, as is the case for non-zero rotation rates. A recirculation zone forms immediately behind the sphere (shown in figure 7) but the streamwise vortices are similar to those observed in the wake when α is negative in that they remain adjacent to the wall and do not merge as they travel downstream. Again, a good agreement is shown between the numerical and experimental flow visualization.

Pressure contours have been plotted in the streamwise centreplane of the sphere for $Re = 100$ and results are shown in figure 8 for the two extremes of rotation rate ($\alpha = 1$ and -1) and for the non-rotating sphere with $\alpha = 0$. In each case the sphere develops a region of high pressure in the upstream gap region, with a negative pressure gradient directed clockwise around the sphere surface. In figure 8(*a*), the magnitude of the centreplane pressure continues to decrease in the clockwise direction around the sphere surface, until a minimum pressure is reached near the downstream wall. For the non-rotating and the reversed rolling spheres (figures 8*b* and 8*c*, respectively) a region of lower pressure develops near the top of the sphere that creates an acceleration of the fluid passing over the top of the sphere. The pressure contours

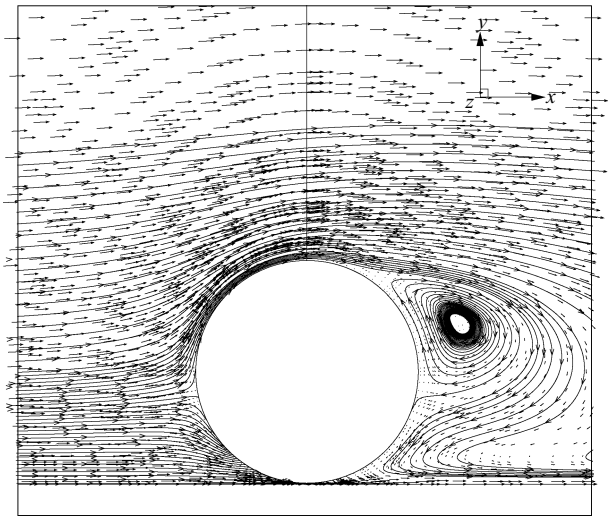

FIGURE 7. Particle traces and velocity vectors showing flow on the symmetry plane for the non-rotating sphere at $Re = 200$.

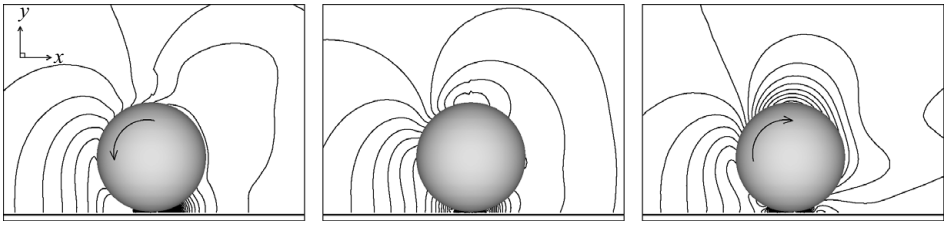

(*a*) $\alpha = 1$. (*b*) $\alpha = 0$. (*c*) $\alpha = -1$.

FIGURE 8. Pressure contours in the $z = 0$ symmetry plane at $Re = 100$ for three different rotation rates.

given in figure 8(*b*) show a very good agreement with those reported by Zeng *et al.* (2005) for the translating sphere at larger distances from the wall.

Within the steady flow regime, the drag coefficient varies with both the rotation rate and the Reynolds number. The viscous and pressure components of the drag are shown in figure 9, along with the total drag coefficient in each case. The viscous component of the drag varies proportionally to the rotation rate at a given Reynolds number and decreases from a maximum at $\alpha = -1$ to a minimum at $\alpha = 1$. The pressure component of the drag displays a more complex relationship with α, where C_{Dp} is higher for $\alpha = 1$ but decreases and approaches a constant value at a given Reynolds number for $\alpha \leqslant 0$. This is a reflection of the fact that the minimum pressure contours of figure 8 are located near the top, rather than at the back, of the sphere for $\alpha \leqslant 0$, and therefore have only a relatively small impact on the value of the streamwise pressure drag.

At all Reynolds numbers considered in this study, the viscous component of the drag force dominates for $\alpha > 0$. However, the values of C_{Dv} and C_{Dp} are comparable for $\alpha \leqslant 0$. These two components of the drag force result in an overall drag coefficient that decreases from a maximum at $\alpha = -1$ to a minimum at $\alpha \approx 0$ and then increases slightly as the rotation rate reaches positive values. For all rotation rates, the coefficient

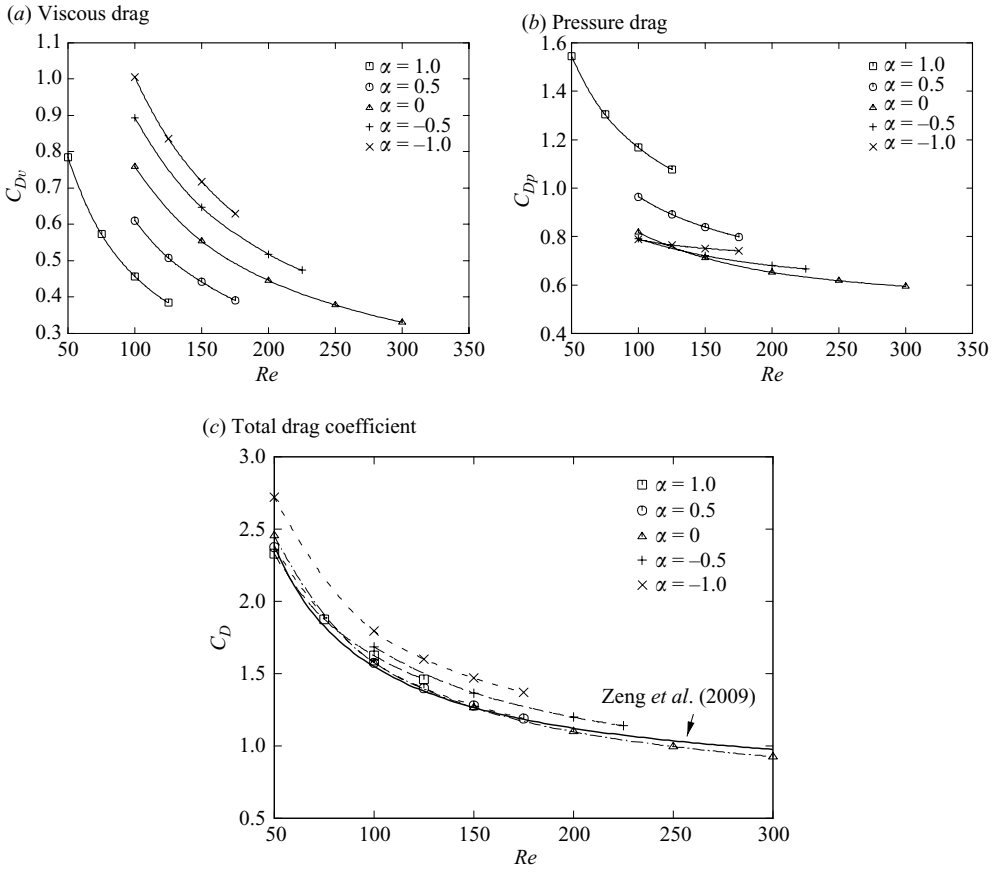

FIGURE 9. Drag coefficient components for the steady flows at various rotation rates.

of drag shows a steady decrease with increasing Reynolds number. Zeng *et al.* (2009) provide an approximate fitting formula for the drag on spheres at various distances from the wall for the non-rotating case. This fit is shown in figure 9. The current predictions lie within 3 % of this fit over the entire range. Zeng *et al.* (2009) indicate that their approximate fit is accurate within 6 %; hence, this provides a useful validation test for the force predictions.

Figure 10 shows the variation of the lift coefficient with Reynolds number for selected values of α in the steady wake regime. As for the drag, Zeng *et al.* (2009) provide an approximate fit for the lift for the non-rotating case. The lift predictions are within their fitting accuracy. Of interest for $\alpha < 0.3$ is that the lift is positive, while for greater values it is negative, and significantly so for $\alpha = 1$. The transition value of $\alpha \simeq 0.3$ corresponds approximately to the case at which the trailing vortex pair shown in figure 4 disappears.

3.2. *The transition between modes*

The steady flow wake structures shown above indicate several significant differences between the forward-rolling sphere flows and those observed for $\alpha < 0$. In Stewart *et al.* (2008), a conceptual regime boundary was defined for $0 < \alpha < 0.5$ to account for the differences observed in the experimental flows at these rotation rates. Figures 4 and 5 indicate that differences in the wake flows are closely linked to the rotation

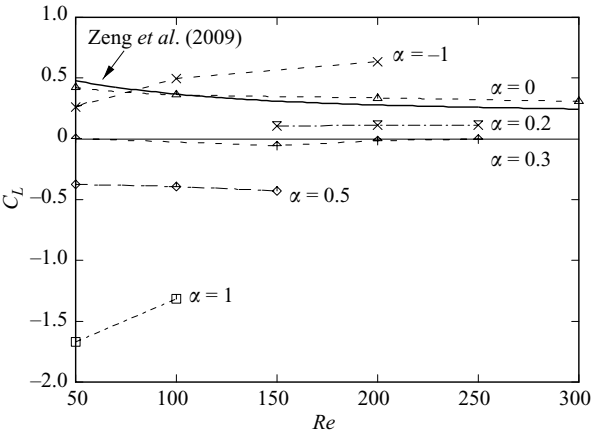

FIGURE 10. Lift coefficient variation with Reynolds number at various rotation rates.

rate of the body. In particular, the numerical simulations indicate that the sphere rotation affects the formation of a recirculation zone immediately behind the body and the development of the streamwise vortex pair. As described above, the wake of the non-rotating sphere has similarities in its placement and the sign of vorticity to that observed when $\alpha < 0$. Consequently, numerical simulations in the range of α between 0 and 0.5 are now used to examine in more detail the apparent transition between modes. These results are shown in figure 11 for the steady flows at $Re = 150$.

Figure 11 shows that as the rotation rate of the sphere is varied from $\alpha = 0.1$ to 0.5, the streamwise vortices that are observed at low and negative rotation rates gradually decrease in strength until $\alpha = 0.4$, when evidence of the streamwise vortices has almost disappeared. At the same time, the recirculation zone directly behind the sphere grows in size. Further increase in the rotation rate to $\alpha = 0.5$ (figure 11*e*) shows a renewed growth in the streamwise vortices but this time the structure is similar to that of figure 4; the wake lifts away from the wall and the sign of the streamwise vorticity changes. To show the change in the flow more clearly, the velocity vectors in the x–y plane at a distance of one diameter downstream of the sphere centre are shown in figure 12.

The vector fields given in figure 12(*a*–*e*) correspond to successive wake visualizations in figure 11. The view in figure 12 is looking upstream, towards the sphere, and the length of the vectors reflects the magnitude of the in-plane velocity. Figure 12(*a*) shows a counter-rotating vortex pair with negative vorticity to the left (directed out of the plane) and positive vorticity to the right. This dipole has an induced motion that causes it to migrate towards the wall. Upon reaching the wall, the vortices separate slightly, according to the manner described by Ersoy & Walker (1985), and this increased lateral displacement reduces the cross-diffusion of vorticity in the downstream wake. This is representative of the flow structures observed for all $\alpha \leqslant 0$. As the rotation rate of the sphere increases from 0.1 to 0.3, the in-plane velocity in figure 11 reduces and the swirling flow behind the sphere almost disappears for $\alpha = 0.3$.

The centre of each vector field in figure 12 corresponds to the point directly downstream of the sphere centre. Figure 12(*b*–*c*) shows that the velocity of the fluid immediately behind the sphere is directed downward, towards the wall. Figure 12(*c*) is close to the transition case where the rotation rate of the sphere has increased

(a) $\alpha = 0.1$.

(b) $\alpha = 0.2$.

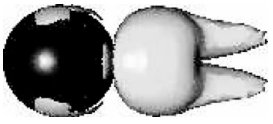

(c) $\alpha = 0.3$.

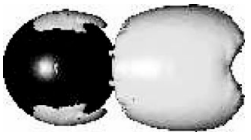

(d) $\alpha = 0.4$.

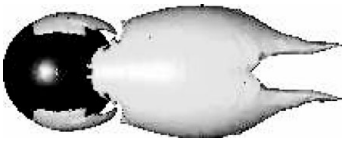

(e) $\alpha = 0.5$.

FIGURE 11. View from above of the wake at intermediate rotation rates and $Re = 150$. The plotted isosurface is the same as in figure 4.

sufficiently to change the sign of the streamwise vorticity in the wake. As the rotation rate of the sphere increases to 0.4, the flow in the sphere wake changes direction to match the imposed motion of the sphere. At higher rotation rates, the flow moves away from the wall and weak vortices form near the top of the sphere. These vortices have a sense of rotation opposite to that described previously, with the left-hand vortex in figure 12(d) being positive and the right-hand vortex being negative. This dipole now has an induced motion towards the free-stream and the weak vortex pair is maintained for only a short distance downstream.

The above results indicate that while the sphere is undergoing rotation rates between 0 and 0.5, a continuous change occurs in the wake. The streamwise vortices either form a dipole that propels towards the wall, where they separate and stabilize, or they form a dipole that moves away from the wall where they rapidly cross-diffuse. The sign of vorticity in these structures can therefore be used to classify the steady flow regime. In the work of Zeng *et al.* (2005), a two-tailed wake is reported for the non-rotating sphere at a fixed distance from the wall. Agreement between their

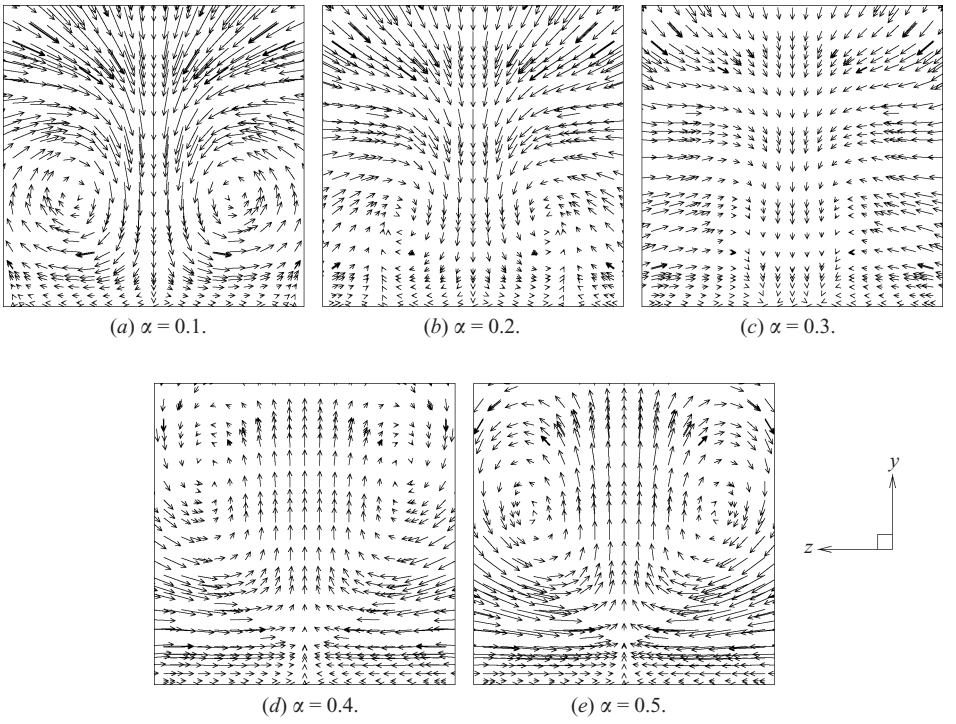

FIGURE 12. Velocity vectors tangent to the plane positioned perpendicular to the flow and located one diameter downstream of the sphere centre. Each viewing frame shows a square of side length one diameter, centred on the sphere.

pressure contours and flow visualization with those of the present study indicates that the same wake mode is observed in both cases when $\alpha = 0$.

3.3. *Unsteady wake modes*

As the Reynolds number of the flow increases, the flow becomes unsteady. Depending on the rotation rate of the sphere, the flow undergoes an unsteady transition in two distinct ways. These are either by the roll-up and shedding of vorticity over the top of the sphere that results in the formation of hairpin vortices (as observed behind the fixed sphere in an unbounded flow), or by the destabilization of the streamwise vortex pair, resulting in a transverse oscillation of the wake downstream of the sphere. The former occurs when the sphere is undergoing forward rolling and the latter occurs for $\alpha \leqslant 0$. Both of these modes were detected during experiments and numerical simulations and are discussed in the following sections.

3.3.1. *The symmetric mode*

The unsteady wake of the sphere that is observed when $\alpha > 0$ is shown in figure 13, with three hairpin vortices that have formed over the top of the sphere and been shed into the wake. The presence of the wall fixes the orientation of the wake and a planar symmetry is present. For this reason, this shedding regime shall be referred to henceforth as the symmetric mode. Numerical wake contours reveal a structure that is very similar to those reported by Johnson & Patel (1999) for the unsteady wake behind a sphere in a free stream and by Zeng *et al.* (2005) for the non-rotating sphere moving in the vicinity of a wall. This latter study provides an interesting comparison

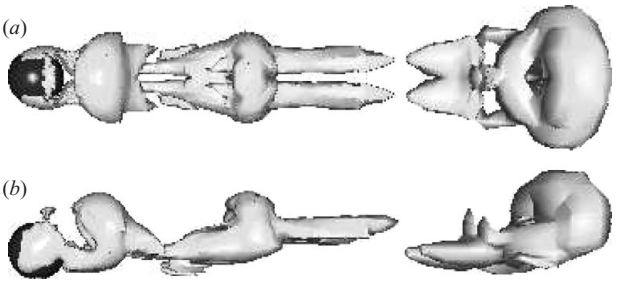

FIGURE 13. Unsteady wake at $Re = 200$ and $\alpha = 1$ showing the shedding of hairpin vortices. Views are from above (a) and the side (b), with the isosurfaces as defined for figure 4.

with the present investigation as the unsteady symmetric mode is observed by them when $\alpha = 0$ for the sphere in the proximity of a wall. In both the experimental results outlined by Stewart *et al.* (2008) and the present numerical simulations, the wake at $\alpha = 0$ remains steady until $Re > 300$; only in the experimental results is a slight cross-stream undulation of the wake observed. This unsteady flow is not characteristic of the onset of the symmetric mode described above, but rather is typical of the antisymmetric mode that shall be discussed in § 3.3.2.

Within the symmetric shedding regime, the presence of the wall prevents the formation of hairpin vortices on the lower (wall) side of the wake. Furthermore, an unsteady flow is observed at lower Reynolds numbers than that for the sphere in unbounded flow, where the critical Reynolds number of transition is commonly quoted at being just above 270 (Magarvey & Bishop 1961; Natarajan & Acrivos 1993; Schouveiler & Provansal 2002). In this way, the imposed rotation acts to enhance the instabilities in the flow. The combined wall vicinity and sphere rotation also acts to vary the Strouhal number of the wake. The sphere in an unbounded flow has a Strouhal number of approximately 0.137 at $Re = 300$ (Johnson & Patel 1999), with Zeng *et al.* (2005) finding values up to 15 % higher when the sphere is at a distance of one diameter from the wall. Results of this study indicate St values in the range 0.110–0.125 for the sphere moving with positive α for Reynolds numbers between 175 and 225. The reduction in the Strouhal number may in part be due to the lower Re at which the flows are recorded, with another possible explanation being the effect of the imposed sphere rotation. A 7 % decrease in St is recorded at $Re = 200$ when the rotation is increased from $\alpha = 0.5$ to 1.

The unsteady wake observed for $\alpha = 1$ remains perfectly periodic over the range of Re studied, with a single frequency present in the wake. This is not true for all rotation rates considered. When $\alpha = 0.5$ and Re increases beyond 210 in the numerical simulations, a second low-frequency component develops. This is illustrated by the two frequency spectra given in figure 14. At $\alpha = 0.5$ and $Re = 212.5$ (figure 14a), the wake is ordered and periodic, with a Strouhal number of 0.120. Increasing the Reynolds number causes a low-frequency mode to grow in the wake, with $St \approx 0.045$. At $Re = 225$ (figure 14b), this mode has become the dominant frequency in the wake.

The two frequency components of figure 14(b) result in a low-frequency modulation in the wake that affects the strength of the hairpin vortices that are shed from the sphere. This is apparent in the time history of the wake-induced drag force on the sphere. Figure 15 gives the variation in C_D for $\alpha = 0.5$ over several periods of the low-frequency mode and the variation in the value of the local maximum drag indicates the shedding of hairpin vortices of varying strength.

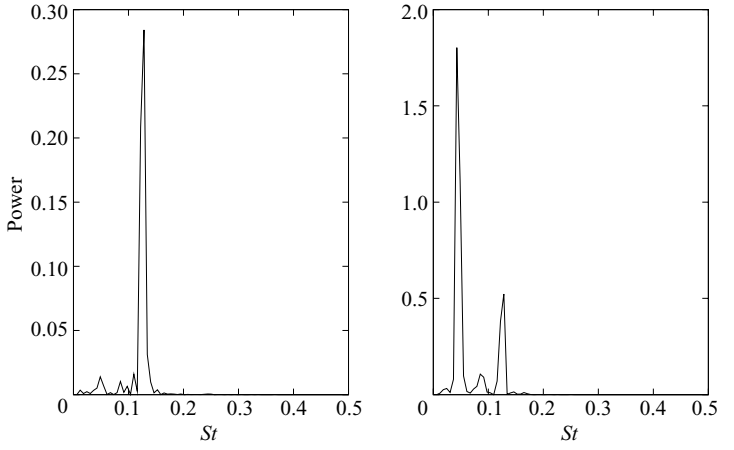

(*a*) The dominant frequency present at $Re = 212.5$. (*b*) Dual spectral peaks at $Re = 225$.

FIGURE 14. Frequency power spectra for $\alpha = 0.5$ showing the development of a low-frequency component as Reynolds number increases.

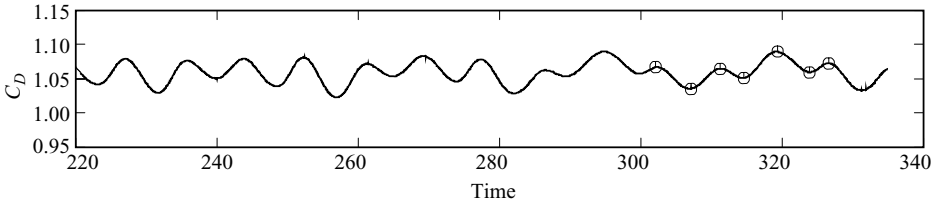

FIGURE 15. Drag-time history for the sphere at $\alpha = 0.5$ and $Re = 225$, showing the effect of multiple frequencies on the wake. The marked symbols indicate selected times corresponding to the isosurface plots in figure 16.

To understand better the effect that the frequency modulation has on the structures in the wake, a series of images has been taken, corresponding to local extrema in the drag force of figure 15. These wake images are given in figure 16 at the sequence of times indicated by the symbols on the drag trace of figure 15 and show the development of the wake over one period of the low-frequency mode. The size and strength of newly formed vortex structures vary considerably with time. As the structures progress downstream, the difference in strength becomes apparent and is reflected in the differing displacements of the vortices from the wall (not shown). A global maximum in the drag occurs at the time of the fifth image in the sequence and the hairpin vortex forming and being shed has a greater strength than those shed before or after. The same structure is shown as the downstream-most vortex structure in the final image, which is almost a repeat of the wake structure given in the first image of the sequence. A similar modulation in the vortex shedding was observed previously during the experimental investigation but at that stage it was unclear whether it was a natural evolution of the wake or a transition brought about by small irregularities in the sphere motion, as described by Stewart *et al.* (2008).

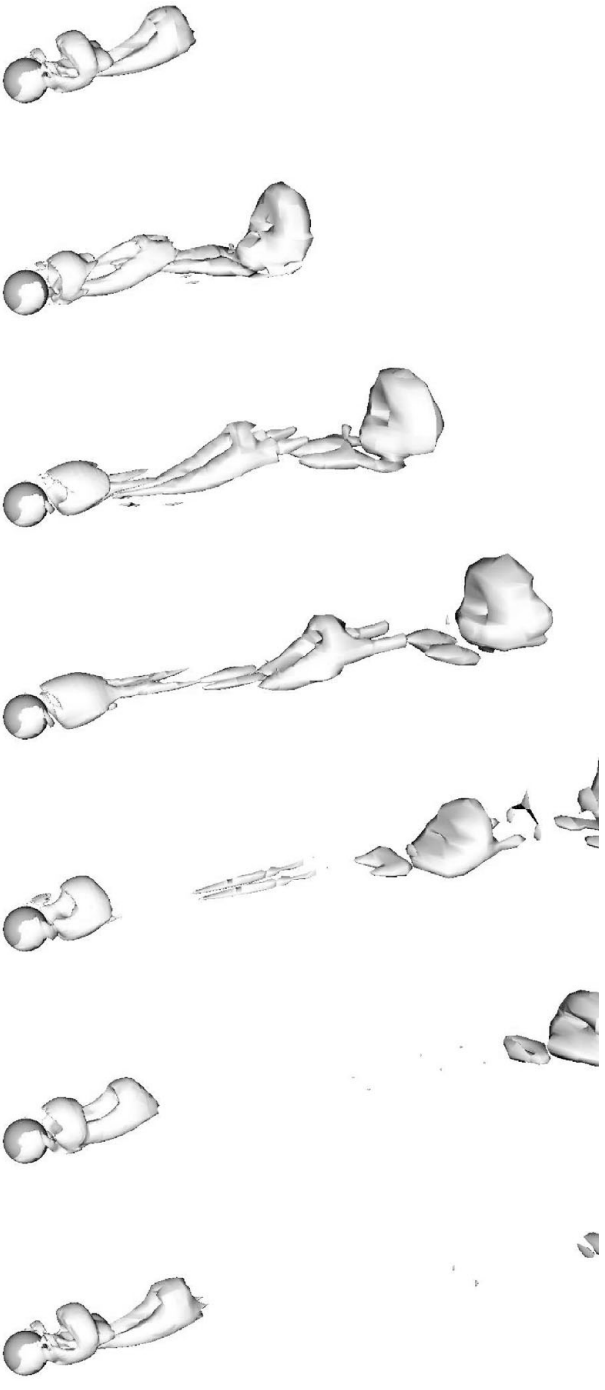

FIGURE 16. Irregular shedding as viewed from the side for $\alpha = 0.5$ and $Re = 225$. Times correspond to those marked in figure 15. The plotted isosurface is the same as in figure 4.

3.3.2. *The antisymmetric mode*

In contrast to the shedding of hairpin vortices described above, a different unsteady mode develops when the sphere is rotating with $\alpha < 0$. This mode manifests itself as a

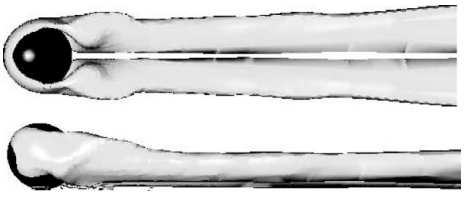

(*a*) Steady wake at $Re = 200$.

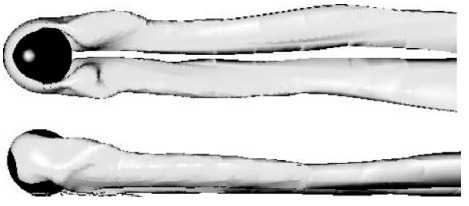

(*b*) Antisymmetric wake after a perturbation has been introduced.

FIGURE 17. Planar-symmetric and sinuous wake modes observed at $\alpha = -1$ and $Re = 200$. The plotted isosurface is as per figure 4.

periodic undulation of the streamwise vortices, with a preferred antisymmetric form. Henceforth, this mode shall be referred to as the antisymmetric mode. During the numerical simulations at higher Re, the unsteady antisymmetric wake mode develops following the introduction of random noise to the three-dimensional velocity field. At a lower Re, this perturbation to the flow has no overall effect and decays rapidly to the steady solution. When this perturbation is added to a steady flow at a higher Re, the unsteady mode develops and converges to a regular periodic wake. Figure 17 shows the two wake modes obtained during simulations at $Re = 200$, both with and without this perturbation to the flow.

Simulations that are allowed to develop from rest without any additional noise exhibit flow that remains steady with a planar symmetry, at least for a considerable time, as shown in figure 17(*a*). This represents an unstable solution, and the addition of random noise accelerates the development of the unsteady mode given in figure 17(*b*). It is possible that the antisymmetric mode of figure 17(*b*) may develop naturally in the simulations if enough time was allowed to elapse. However, the computing requirements needed to test this theory are prohibitive. The flows obtained via the introduction of random noise closely match those observed in experiments, where a low level background turbulence is unavoidable. The positions of the vortical structures at the front and sides of the sphere do not change in figures 17(*a*) and 17(*b*). It is only in the near wake that the disturbance of the vortices in the periodic wake becomes apparent.

Initially, the perturbation added to the flow of figure 17(*a*) appears as a transverse undulation in the wake, similar to that observed behind a freely falling sphere in an unbounded flow (Magarvey & Bishop 1961). While the wake of figure 17(*b*) has lost its symmetry, the deformation over time is still relatively small and the major motion of the streamwise vortices lies in a plane parallel to the wall. The resulting sinuous motion of the wake creates a net transverse force on the sphere, the coefficient of which is defined in a manner similar to the drag coefficient and is denoted by C_Z.

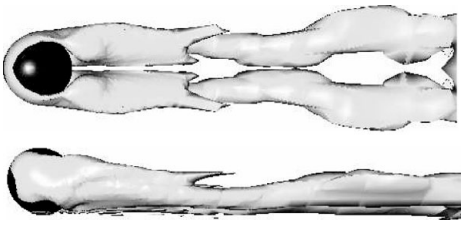

(*a*) Unstable symmetric wake mode at $Re = 300$.

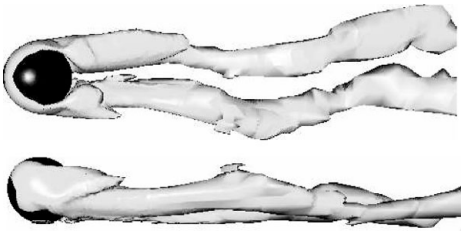

(*b*) Stable antisymmetric wake mode following a perturbation to the flow.

FIGURE 18. Wake modes for $\alpha = -1$, $Re = 300$, showing the two possible unsteady modes that exist prior to, and following, a white noise perturbation to the flow. The plotted isosurface is as per figure 4.

When the Reynolds number of the simulations increases further for $\alpha = -1$, an interesting discovery is made. The flow undergoes a bifurcation to an unstable solution branch that is not detected in the experiments. In the simulations, when allowed to develop in the absence of any noise, the reversed rolling wake develops into an unsteady symmetric mode. This mode remains planar symmetric for many cycles; however, when this wake is fully developed, the introduction of a small perturbation is enough to cause the transition to the antisymmetric mode observed in experiments. Presumably, the symmetric wake state is weakly unstable and it would naturally undergo transition to the sinuous state given sufficient time, even without the applied perturbation. Figure 18 shows the structure of these two unsteady modes with the planar symmetry clearly apparent in figure 18(*a*).

Figure 18(*a*) shows a distinctive symmetric kinking in the wake, while figure 18(*b*) displays the antisymmetric mode observed in experiments. It is interesting to note that the kinking of the wake similar to that in figure 18(*a*) has been repeatedly observed in the asymmetric wake behind a sphere in an unbounded flow (Sakamoto & Haniu 1995; Ormières & Provansal 1999; Schouveiler & Provansal 2002) and has been described as the initial stages of the unsteady wake prior to the shedding of hairpin vortices. Compared with the sinuous wake at $Re = 200$ (figure 17*b*), the antisymmetric wake at $Re = 300$ develops a significant motion in the direction normal to the wall, with alternating sides of the wake lifting away from the boundary. In the simulations of Zeng *et al.* (2005), a symmetry condition was imposed along the streamwise centreplane of the sphere, thereby preventing the development of any antisymmetric wake modes. However, the symmetric kinking mode of figure 18(*a*) was also absent in their simulations, and it is likely that this form only develops within a certain critical distance close to the wall and when $\alpha < 0$.

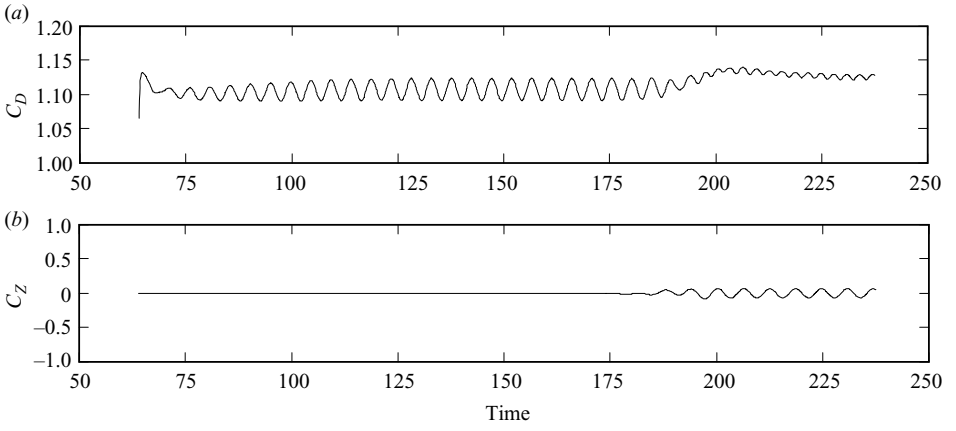

FIGURE 19. Section of the drag and transverse force–time histories for $\alpha = -1$, $Re = 300$.

The development of the antisymmetric mode at $Re = 300$ is shown in the force–time histories of figure 19, following the introduction of the perturbation to the flow at $\tau = 150$. This leads to the development of an oscillatory cross-stream force. As the amplitude of C_Z grows, the amplitude of the fluctuating drag rapidly decreases. The frequency of the unsteady drag force also alters until it is twice that of the transverse force when the antisymmetric mode is fully developed.

When the sphere has no net rotation, the steady, streamwise vortex pair is observed in the wake. This wake structure lends itself to the antisymmetric type of instability, rather than the symmetric mode observed by Zeng *et al.* (2005) when the sphere is positioned farther from the wall. However, no unsteady flow was detected in the numerical simulations at the upper Reynolds number limit of $Re = 300$. Experimental results showed an unsteady undulation in the wake that is first apparent at $Re \approx 300$, as reported by Stewart *et al.* (2008).

From potential flow theory, the two streamwise vortices near a wall can be considered as part of a four vortex system. The two visible vortices have an induced motion from each other, as well as from the effect of their image vortices located on the wall. Such systems have been analysed in the wake of aircraft and have been found to lead to a range of possible instabilities with various wavelengths (Crouch 1997; Fabre, Jacquin & Loof 2002; Jacquin *et al.* 2003). Following observations of the antisymmetric mode in the direction perpendicular to the wall, it is concluded that the streamwise vortices do not remain oriented in a single, inclined plane. Rather, it is apparent that alternating sides of the wake lift away from the wall and the point of maximum lateral displacement is not the same as the location of maximum vertical displacement. This fact, in conjunction with the sinuous motion observed from above, leads to the conclusion that the wake is composed of two spiral vortices that wind in opposite directions and are out of phase by half a wavelength.

3.3.3. *Experimental comparison of the unsteady wake*

When compared with the experimental results, the simulations show a good agreement as to the structures observed in the sphere wake. Numerical results are shown, along with dye visualizations from the experiments in figures 20 and 21 for the unsteady flow regimes. Figure 20 shows the shedding of hairpin vortices behind the forward-rolling sphere at $Re = 200$. The visualization method of Jeong & Hussain (1995) used in the simulations shows the vortical structures to be upright and almost

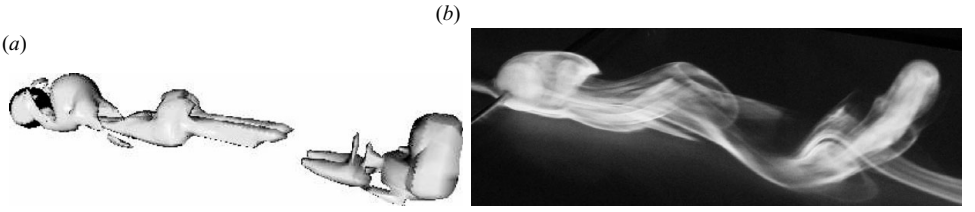

FIGURE 20. Forward-rolling sphere at $Re = 200$.

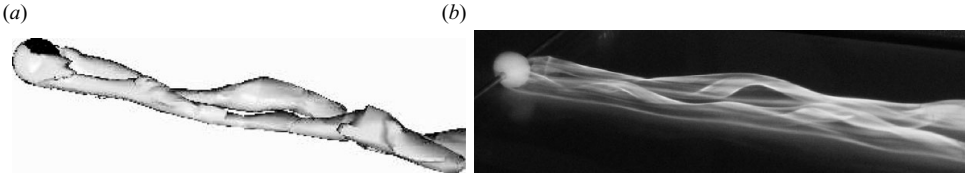

FIGURE 21. Reversed rolling sphere at $Re = 300$ (a) and 200 (b).

perpendicular to the wall, in contrast to the experimental dye method, which does not capture as accurately the regions of vorticity downstream.

Of the two instabilities predicted in the numerical simulations for the reverse rolling sphere wake, only the antisymmetric mode is observed in experiments. The antisymmetric wake mode is shown in figure 21 behind the reverse rolling sphere with $\alpha = -1$. The experimental results are shown at $Re = 200$, while the numerical flows are at $Re = 300$. During the numerical simulations, the onset of an unsteady flow appears to be delayed compared with the experiments and at $Re = 200$ the simulations indicate a flow that is just above the critical Reynolds number of transition to the unsteady flow. The spiral motion of the streamwise vortices is more clearly distinguished in the experimental dye visualization of figure 21.

The Strouhal number obtained from the unsteady numerical simulations is plotted in figure 22. Experimental data taken from Stewart *et al.* (2008) are shown for comparison and the dashed lines indicate the trend for each set of numerical results. When $\alpha < 0$ (figures 22*a* and 22*b*), the simulations show that decreasing the magnitude of rotation decreases the wake frequency. This trend is also present in the experimental results. However, the numerical data consistently overestimate the experimental results. Numerical simulations indicate that this difference is unlikely to be due to differences in the gap ratio during simulations and experiments. A series of simulations was run with a gap ratio equal to 5 % of the diameter. This value is thought to more accurately reflect the gap ratio present in experiments when $\alpha < 0$. However, the simulations at this larger gap ratio reveal a decrease in St of less than 1 % for $\alpha = -1$. A more likely explanation for the lower experimental Strouhal numbers is therefore that the difference in Strouhal number is due to the effect of the supporting rod in the experiments, which has been shown to alter the Strouhal number for the wake of a sphere in an unbounded flow.

Both the numerically predicted and the observed values of St in figures 22(a) and 22(b) appear to be fairly independent of changes in Re. However, the critical Reynolds number of transition to unsteady flow differs, and at $Re = 225$, the numerical simulations provided a steady flow solution for $\alpha = -0.5$, even following the addition

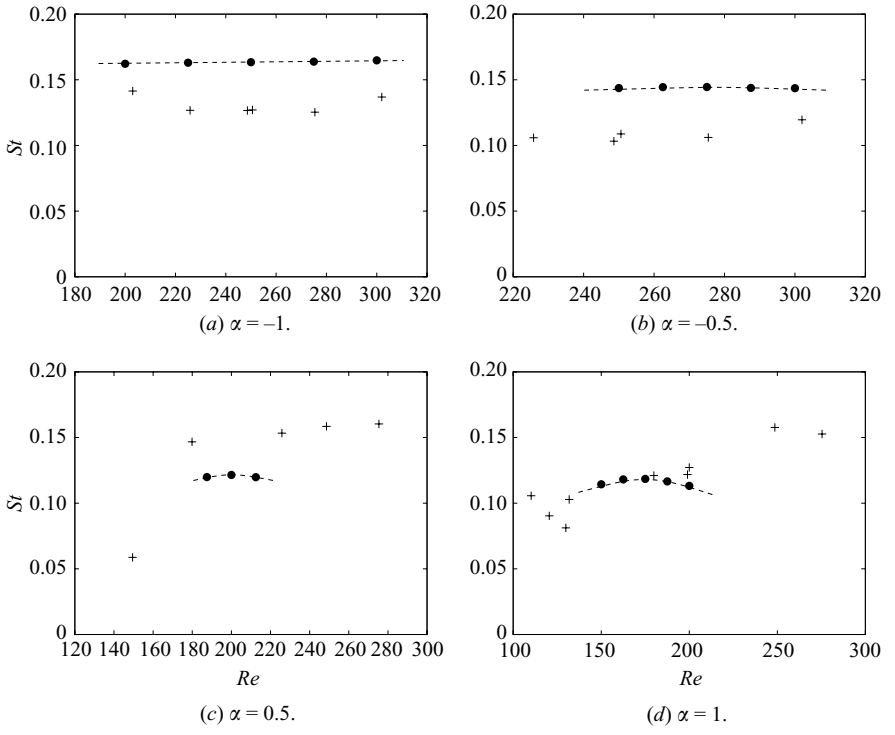

FIGURE 22. Comparisons of the experimental (+) and numerical (●) wake frequencies for the four nonzero rotation rates. Dashed lines represent the trends of the numerical data.

of noise to the solution. The transition to unsteady flow in the simulations takes place at higher Re than that in the experiments.

For $\alpha > 0$, the magnitude of St from the numerical simulations shows a reasonable agreement with the experiments and the numerical data fall within the experimental range. However, the simulations indicate that the onset of unsteady flow again occurs at higher Re than that in experiments. For $\alpha = 1$, this onset occurs at $125 < Re < 150$ and for $\alpha = 0.5$, the transition takes place when $175 < Re < 187$. Unlike the experimental data, which show an increasing trend with Re, the numerical simulations for the forward-rolling sphere provide St values that are nearly constant and lie in the region of $St \approx 0.12$, independent of the rotation rate. This is somewhat lower than the values of 0.136 and 0.137 obtained by Tomboulides & Orszag (2000) and Johnson & Patel (1999) for the wake of a sphere in an unbounded flow at $Re = 300$.

Zeng *et al.* (2005) found an increase in St as the sphere approaches the wall; however, no gap ratios below 25 % of the diameter were considered in their study and no conclusions were reached as to how St may vary in the region very close to the wall. Although the investigation of Zeng *et al.* (2005) focuses on the non-rotating sphere, they find that the unsteady wake involves the shedding of hairpin vortices in the symmetric mode at a gap ratio of $0.5D$. During this shedding process, they calculate a Strouhal number of approximately 0.15 at $Re = 270$. This is in reasonable agreement with the St values plotted in figures 22(c) and 22(d), but varies quite differently to those for $\alpha < 0$, for which a different mode is observed.

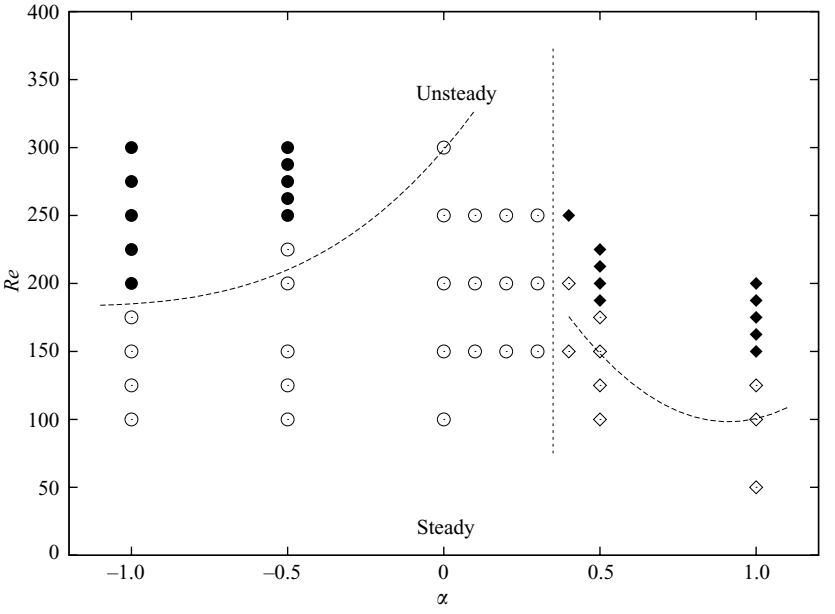

FIGURE 23. Transition map of the four different wake modes predicted by the simulations. The dashed curves indicate the approximate regime boundaries as determined by experiments and published in Stewart *et al.* (2008). Filled symbols indicate unsteady flow and open symbols indicate steady flow. In addition, the circles indicate the trailing counter-rotating vortex pair self-advects towards the wall, and the diamond symbols indicate that the pair has swapped sign so that self-advection is away from the wall.

3.4. *Regime diagram*

The parameter space given in figure 23 indicates the regions in which the different wake modes are observed in the numerical simulations. Steady modes are shown by open symbols and the transition to unsteady flow (closed symbols) occurs as Re increases. The dashed curves in figure 23 represent the mode limits determined from experimental results, as published by Stewart *et al.* (2008), and the vertical line indicates a generalized boundary between the wake modes as determined from the numerical simulations at intermediate rotation rates. Figure 23 shows some differences to the experimental parameter space identified by Stewart *et al.* (2008) and it appears that the Reynolds number threshold for instability decreases slightly due to the presence of the supporting rod in the experiments. The same wake modes have been detected in each case, although the numerical simulations show a delay in the onset of unsteady flow to higher Reynolds numbers.

The two separate steady flow regimes are the result of the changing sign of streamwise vorticity in the wake. The mode observed when $\alpha > 0$ is the least stable, with a transition to unsteady flow occurring at $Re < 150$ for $\alpha = 1$. A change in the steady wake mode occurs for $\alpha \approx 0.35$, and for negative values of α the steady wake may develop into the unsteady antisymmetric mode at higher Reynolds numbers. The sliding sphere with $\alpha = 0$ displays the most stable configuration, and the transition to unsteady flow is not observed in the simulations. This is true for Reynolds numbers up to 350, even following the introduction of a perturbation to the flow. In contrast,

the sphere in a free-stream flow undergoes a transition to unsteady flow at $Re \approx 270$ (Thompson *et al.* 2001). For the larger magnitude, negative values of α, the transition Re reduces to $Re \approx 185$ for $\alpha = -1$.

4. Conclusions

A good qualitative agreement has been found between the experimental and numerical wake formations behind the rolling sphere. Four distinct wake modes are identified: two steady and two unsteady. These wake modes are strongly dependent on the rotation rate of the sphere. Furthermore, the steady modes observed maintain a planar symmetry that is fixed perpendicular to the wall and passes through the sphere centre. Forward rolling of the sphere creates a compact zone of recirculating fluid that undergoes a transition to the shedding of hairpin vortices as the Reynolds number increases. When reversed rolling is imposed, the wake takes the form of a streamwise vortex pair that originates at the sides of the sphere for $\alpha < 0$, and at the rear of the body for $\alpha = 0$. These streamwise vortices undergo a transition to an antisymmetric wake mode as Re increases.

The unsteady, antisymmetric wake mode occurring behind the sphere for $\alpha < 0$ is a new mode. From observations and images of the flow, it is concluded that the wake is composed of two spiral vortices that wind in opposite directions and are half a wavelength out of phase. This motion results in a sinuous motion of the vortex cores when viewed from above. The axes of these spirals are not quite parallel in the streamwise direction, as there is a slight divergence of the wake downstream.

Numerical simulations provide additional information about the structure of these steady and unsteady wake modes. Visualizations of the vorticity for $\alpha > 0$ show that the wake has a structure that closely resembles the double tail, although on a reduced scale and displaced farther from the wall. A numerical examination of intermediate rotation rates between 0.1 and 0.5 indicates that the two steady modes undergo a smooth and continuous transition. The steady streamwise structures in the wake form a counter-rotating pair, but the sign of vorticity changes depending on the magnitude of the sphere rotation.

In addition to the wake modes described above, the numerical simulations reveal an unstable bifurcation in the solutions for the unsteady wake at $\alpha < 0$. When the flow develops with no background turbulence or external perturbation, a symmetric mode is possible. This unstable symmetric mode displays a kinking of the streamwise vortices in the wake. The introduction of a small perturbation to this flow brings about a transition to the antisymmetric wake mode observed in experiments.

From this study it has been possible to extend the current knowledge of bluff body wake transitions when under the influence of a nearby wall and body rotation. During the present investigation these two effects act in competition, with the wall acting to stabilize the flow while increasing sphere rotation acts to destabilize it. From here, it is intended that this work shall be extended to lower Reynolds numbers, where further applications exist in the study of biological fluid flows.

The authors wish to gratefully acknowledge the support of a Monash University Postgraduate Publication Award as well as Australian Research Council Discovery Grants DP0877327 and DP0877517 and computing time from the Australian Partnership for Advanced Computing.

REFERENCES

Ashmore, J., del Pino, C. & Mullin, T. 2005 Cavitation in a lubrication flow between a moving sphere and a boundary. *Phys. Rev. Lett*. **94**, 124501 (1–4).

Cherukat, P. & McLaughlin, J. B. 1990 Wall-induced lift on a sphere. *Intl J. Multiphase Flow* **16** (5), 899–907.

Cherukat, P. & McLaughlin, J. B. 1994 The inertial lift on a rigid sphere in a linear shear flow field near a flat wall. *J. Fluid Mech.* **263**, 1–18.

Chorin, A. J. 1968 Numerical solution of the Navier–Stokes equations. *Math. Comput*. **22**, 745–762.

Cox, R. G. & Hsu, S. K. 1977 The lateral migration of solid particles in a laminar flow near a plane. *Intl J. Multiphase Flow* **3**, 201–222.

Crouch, J. D. 1997 Instability and transient growth for two trailing-vortex pairs. *J. Fluid Mech* **350**, 311–330.

Ersoy, S. & Walker, J. D. A. 1985 Viscous flow induced by counter-rotating vortices. *Phys. Fluids* **28** (9), 2687–2698.

Fabre, D., Jacquin, L. & Loof, A. 2002 Optimal perturbations in a four-vortex aircraft wake in counter-rotating configuration. *J. Fluid Mech.* **451**, 319–328.

Ghidersa, B. & Dušek, J. 2000 Breaking of axisymmetry and onset of unsteadiness in the wake of a sphere. *J. Fluid Mech.* **423**, 33–69.

Humphrey, J. A. C. & Murata, H. 1992 On the motion of solid spheres falling through viscous fluids in vertical and inclined tubes. *Transactions ASME: J. Fluids Engng* **114**, 2–11.

Jackson, S. P. 2007 The growing complexity of platelet aggregation. *Blood* **109** (12), 5087–5095.

Jacquin, L., Fabre, D., Sipp, D., Theofilis, V. & Vollmers, H. 2003 Instability and unsteadiness of aircraft wake vortices. *Aerosp. Sci. Technol*. **7**, 577–593.

Jeong, J. & Hussain, F. 1995 On the identification of a vortex. *J. Fluid Mech.* **285**, 69–94.

Johnson, T. A. & Patel, V. C. 1999 Flow past a sphere up to a Reynolds number of 300. *J. Fluid Mech.* **378**, 19–70.

Karniadakis, G. E., Israeli, M. & Orszag, S. A. 1991 High-order splitting methods for the incompressible Navier–Stokes equations. *J. Comput. Phys.* **97**, 414–443.

Leontini, J. S., Thompson, M. C. & Hourigan, K. 2007 Three-dimensional transition in the wake of a transversely oscillating cylinder. *J. Fluid Mech.* **577**, 79–104.

Liu, Y. J., Nelson, J., Feng, J. & Joseph, D. D. 1993 Anomalous rolling of spheres down an inclined plane. *J. Non-Newtonian Fluid Mech.* **50**, 305–329.

Magarvey, R. H. & Bishop, R. L. 1961 Transition ranges for three-dimensional wakes. *Can. J. Phys.* **39**, 1418–1422.

Mittal, R. 1999 Planar symmetry in the unsteady wake of a sphere. *AIAA J.* **37** (3), 388–390.

Natarajan, R. & Acrivos, A. 1993 The instability of the steady flow past spheres and disks. *J. Fluid Mech.* **254**, 323–344.

Ormières, D. & Provansal, M. 1999 Transition to turbulence in the wake of a sphere. *Phys. Rev. Lett*. **83** (1), 80–83.

Prokunin, A. N. 2004 Microcavitation in the slow motion of a solid spherical particle along a wall in a fluid. *Fluid Dyn.* **39** (5), 771–778.

Prokunin, A. N. 2007 The effects of atmospheric pressure, air concentration in the fluid, and the surface roughness on the solid-sphere motion along a wall. *Phys. Fluids* **19**, 113601 (1–10).

Ryan, K., Thompson, M. C. & Hourigan, K. 2005 Three-dimensional transition in the wake of bluff elongated cylinders. *J. Fluid Mech.* **538**, 1–29.

Ryan, K., Thompson, M. C. & Hourigan, K. 2007 The effect of mass ratio and tether length on the flow around a tethered cylinder. *J. Fluid Mech.* **591**, 117–144.

Sakamoto, H. & Haniu, H. 1995 The formation mechanism and shedding frequency of vortices from a sphere in uniform shear flow. *J. Fluid Mech.* **287**, 151–171.

Schouveiler, L. & Provansal, M. 2002 Self-sustained oscillations in the wake of a sphere. *Phys. Fluids* **14** (11), 3846–3854.

Seddon, J. R. T. & Mullin, T. 2008 Cavitation in anisotropic fluids. *Phys. Fluids* **20** (2), 023102 (1–5).

Sheard, G. J., Thompson, M. C. & Hourigan, K. 2004 From spheres to circular cylinders: non-axisymmetric transitions in the flow past rings. *J. Fluid Mech.* **506**, 45–78.

Stewart, B. E. 2008 The dynamics and stability of flows around rolling bluff bodies. PhD thesis, Monash University.

Stewart, B. E., Leweke, T., Hourigan, K. & Thompson, M. C. 2008 Wake formation behind a rolling sphere. *Phys. Fluids* **20**, 071704 (1–4).

Takemura, F. & Magnaudet, J. 2003 The transverse force on clean and contaminated bubbles rising near a vertical wall at moderate Reynolds number. *J. Fluid Mech.* **495**, 235–253.

Taneda, S. 1956 Experimental investigation of the wake behind a sphere at low Reynolds numbers. *Phys. Soc. Japan* **11** (10), 1104–1108.

Thompson, M. C., Hourigan, K., Cheung, A. & Leweke, T. 2006 Hydrodynamics of a particle impact on a wall. *Appl. Math. Model.* **30**, 1356–1369.

Thompson, M. C., Leweke, T. & Provansal, M. 2001 Kinematics and dynamics of sphere wake transition. *J. Fluids Struct.* **15**, 575–585.

Tomboulides, A. G. & Orszag, S. A. 2000 Numerical investigation of transitional and weak turbulent flow past a sphere. *J. Fluid Mech.* **416**, 45–73.

Woollard, K. J., Suhartoyo, A., Harris, E. E., Eisenhardt, S. U., Jackson, S. P., Peter, K., Dart, A. M., Hickey, M. J. & Chin-Dusting, J. P. F. 2008 Pathophysiological levels of soluble p-selectin mediate adhesion of leukocytes to the endothelium through mac-1 activation. *Circulat. Res.* **103** (10), 1128–1138.

Zeng, L., Balachandar, S. & Fischer, P. 2005 Wall-induced forces on a rigid sphere at finite Reynolds number. *J. Fluid Mech.* **536**, 1–25.

Zeng, L., Najjar, F., Balachandar, S. & Fischer, P. 2009 Forces on a finite-sized particle located close to a wall in a linear shear flow. *Phys. Fluids* **21**, 033302 (1–18).